Multi-Site Cross Calibration on the LAPAN-A3/IPB Satellite Multispectral Camera with One-Dimensional Kalman Filter Optimization

Sartika Salaswati[1], Adhi Harmoko Saputro[2], Wahyudi Hasbi[3], Deddy El Amin[4], Patria Rachman Hakim[5], Silmie Vidiya Fani[6], Agung Wahyudiono[7], Ega Asti Anggari[8]
Department of Physics, Faculty of Mathematics and Natural Sciences, University of Indonesia, Indonesia[1, 2]
Research Center for Satellite Technology, National Research and Innovation Agency (BRIN), Indonesia[1, 3, 4, 5, 7, 8]
Research Center for Space, National Research and Innovation Agency (BRIN), Indonesia[6]

***Abstract*—Multispectral cameras on remote sensing satellites must have good radiometric quality due to their wide range of applications. One type of radiometric calibration that can be performed while the satellite is in orbit is cross-calibration. This research focuses on cross-calibration because it has advantages, including being cost-effective and capable of frequent execution. We proposed a multi-site cross-calibration method with two reference cameras using six calibration sites in 2023. The LISA LAPAN-A3 (LA3) camera serves as the target camera, while the OLI LANDSAT-8 (OL8) and MSI SENTINEL-2 (MS2) cameras act as the reference cameras. The calibration process results in numerous calibration coefficients for each channel, thus requiring optimization to produce a single calibration coefficient. The optimization process uses a one-dimensional Kalman filter to reduce measurement noise. The results show that the one-dimensional Kalman filter can reduce noise in the calibration coefficient data, making LA3 radiance values closer to the reference radiance values. Additionally, this study demonstrates that LA3 calibration results with MS2 as the reference camera are better than those with OL8 as the reference.**

Keywords*—Cross-calibration; multi sites; multispectral camera; LAPAN-A3/IPB Satellite; LISA LAPAN-A3 (LA3); OLI LANDSAT-8 (OL8); MSI/SENTINEL-2 (MS2); one-dimensional Kalman filter

I. Introduction

Line Imager Space Application (LISA) is a multispectral camera on the LAPAN A3/IPB satellite. This camera is the main payload that supports the remote sensing mission of the LAPAN-A3/IPB satellite. This camera has blue, green, red, and near-infrared (NIR) channels, with a ground resolution of 15 meters and 120 km swath-width from 510 km altitude. Besides, this camera has 16-bit radiometric resolution and 21 days of temporal resolution [1].

Multispectral cameras on satellites are extensively utilized in remote sensing applications, encompassing the detection and characterization of agroforestry systems [2], evaluation of land-use changes [3], identification of terrestrial vegetation [4], mapping of mangrove forests [5], assessment of forest restoration [6], bamboo mapping [7], and evaluation for sustainable urban development [8].

LISA LAPAN-A3 (LA3), similar to the multispectral cameras used in other remote sensing satellites, serves multiple purposes, including the identification of plant types and growth conditions [9], monitoring drought areas [10], calculating chlorophyll in plants [11], monitoring rice fields [12], and performing land use analysis [13].

This camera produces images consisting of a collection of pixels with specific values. The values in these pixels are called digital numbers (DN). Digital numbers represent the radiometric values of objects in an image [14]. However, calibration coefficients are needed to convert the digital number (DN) values to obtain TOA radiance or TOA reflectance. An absolute radiometric calibration process is required to generate calibration coefficients for the images.

There are several methods of absolute radiometric calibration, including the on-board calibration method [15][16], the Rayleigh calibration method [17][18][19], the vicarious calibration method [16][20][21][22][23], and the cross-calibration method [16][24][25]. Based on previous literature reviews, the cross-calibration method is considered an efficient alternative as it has the advantage of being low cost, high calibration frequency, and can be carried out repeatedly to obtain calibration coefficients for each channel [26].

Furthermore, research on cross-calibration of satellite cameras has been widely conducted. Lu researched cross-calibration for medium-resolution multispectral cameras with large angles [24]. Gao researched cross-calibration to monitor VNIR sensor degradation on the Gaofen-4/GF-4 satellite using three reference sensors, namely OLI/Landsat-8, MSI/Sentinel 2, and MODIS/Terra [25]. Jie Han researched cross-calibration based on a radiometric block adjustment (RBA) algorithm to minimize radiometric effects due to differences in integration time [27]. Mizuochi researched cross calibration with inter-band calibration on a hyperspectral camera [28]. Kohei Arai researched cross-calibration based on vicarious calibration measurements [29]. Due to the significant developments related to this method, this study will also develop a radiometric calibration method based on cross-calibration.

The LA3 calibration has been the subject of numerous investigations. Laboratory calibration [30], vicarious calibration at the Kupang cement mine [31], and Jaddih Hill Madura [32][33] are some of the studies that fall under this category. Although these investigations have yielded calibration

coefficients, the current calibration methods still have drawbacks.

Additionally, the calibration coefficients for satellites need to be updated because there is a possibility that satellites degrade over time. Therefore, other methods are required to complement previous research. This study proposes a multi-site cross-calibration method for the LA3 camera with one-dimensional Kalman Filter for the optimization process. This method is a cross-calibration technique developed from several previously reviewed references. The proposed method differs from the usual cross-calibration techniques because this method uses more than one calibration site, and the calibration coefficients are optimized using the Kalman Filter, resulting in a single final calibration coefficient.

In this study, cross-calibration was also performed using two types of reference cameras, namely, OLI LANDSAT-8 (OL8) and MSI SENTINEL-2 (MS2). The calibration coefficients from these two references were then validated using a cross-validation method, so the calibration result of LA3 with OL8 reference was validated with MS2, and the calibration result of LA3 with MS2 reference was validated with OL8. This research aims to determine if this method can be successfully implemented on the LAPAN-A3/IPB satellite's multispectral camera, resulting in radiance values that are closely comparable to the standard values. This method is expected to complement previous methods and should be applied to the LA3 camera periodically.

II. Descriptions of Calibration Sites and Datasets

A. Calibration Sites

In this study, six sites were used: five in North Africa and one in France. The sites in North Africa are Libya 1, Libya 4, Algeria 3, Mauritania 1, and Mauritania 2. The site in France is the La Crau calibration site. Libya-1, Libya-4, and Algeria-3 are deserts with dunes 100 meters high and a spatial variability of <3% over 100 km. Mauritania 1 and 2 have lower spatial variability compared to the others. The La Crau site has a spatial variability of <3% and a temporal variability of <2% over an area of <20 km [34].

La Crau is one of the RadCalNet calibration sites that provides free radiometric data. The data available includes TOA reflectance, continuously updated every 30 minutes and at a sampling interval of 10 nm within the 380 nm – 2500 nm spectral range. Each site has automated instruments that can generate reflectance and atmospheric data for that site. The provided data is guaranteed in terms of quality and consistency according to international standards [35]. According to research by Revel et al., this area is more heterogeneous than the Gobabeb site in Namibia, a desert [36]. Table I contains the list of calibration sites used in this study.

TABLE I. Calibration Sites

	Sites	Latitude (°)		Longitude (°)	
		Max	***Min***	***Max***	***Min***
PICS	Algeria-3	30.50	30.20	7.60	7.30
	Libya-1	24.80	24.50	13.60	13.30
	Libya-4	28.65	28.42	23.02	22.80
	Mauritania-1	19.60	19.40	-9.20	-9.40
	Mauritania-2	20.60	20.40	-8.50	-8.80
Rad-Cal-Net	La Crau, France	43.56	43.55	4.86	4.86

B. Datasets

The images used in this study are from the LA3 camera as the target camera, and from the OL8 and MS2 cameras as reference cameras. The images are from the calibration sites mentioned earlier, taken in 2023. There are 8 images with 66 pairs of ROIs used for each reference camera.

LA3 is a multispectral camera on the LAPAN-A3 satellite with a wavelength range of 410 nm – 900 nm. This camera consists of four channels: red, green, blue, and NIR. It has a resolution of 15 m, a swath width of 120 km, and a revisit time of 21 days. Based on these specifications, OL8 and MS2 were selected as reference cameras because their specifications are quite similar to those of the LA3 camera.

OL8 is a multispectral camera on the LANDSAT-8 satellite with a wavelength range of 430 nm – 2290 nm. This camera consists of 8 channels with a resolution of 30 m and 1 channel with a resolution of 15 m. The 8 channels with a resolution of 30 m include coastal aerosol, blue, green, red, NIR, SWIR1, SWIR2, and cirrus. The 15 m resolution channel is the panchromatic channel. The camera has a swath width of 185 km and a revisit time of 16 days [37] [38].

MS2 is a multispectral camera on the SENTINEL-2 satellite with a wavelength range of 442 nm – 2202 nm. This camera consists of four channels with a resolution of 10 m, six channels with a resolution of 20 m, and three channels with a resolution of 60 m. SENTINEL-2 is a satellite that consists of two identical twin spacecraft in the same orbit with a 180° phase difference. This satellite's revisit period of five days is relatively short due to the presence of two twin satellites. The mission of this satellite is a multispectral imaging mission with a swath width of 290 km [39]. Table II displays the specs for the reference and target cameras at RGBN wavelengths.

TABLE II. Specifications for Multispectral Cameras on Satellites

Specifications	**OLI/Landsat 8**	**MSI/Sentinel 2**	**LISA/LAPAN-A3**
Resolution	30 m	10 m	15 m
Swath Width	185 km	290 km	120 km
Spectral			
Red	0.64 – 0.67 µm	0.65 – 0.68 µm	0.63 – 0.70 µm
Green	0.53 – 0.59 µm	0.54 – 0.58 µm	0.51 – 0.58 µm
NIR	0.85 – 0.88 µm	0.78 – 0.90 µm	0.77 – 0.90 µm

Additionally, reflectance data from the spectral library and aerosol optical depth data from the AERONET site are used as supporting data. Reflectance data—specifically, desert reflectance—is taken from the spectral library. The region nearest to the calibration sites is where the aerosol data is derived from. These two data sets serve as inputs for the MODTRAN software to generate the surface reflectance of the calibration sites.

III. CALIBRATION METHOD

The proposed calibration method is a cross-calibration technique with radiometric parameters using several internationally standardized calibration sites (multi-sites). The image acquisition of these sites was conducted throughout 2023. Two reference cameras, OL8 and MS2, are also used in this procedure. Fig. 1 displays the block diagram for the multi-site cross-calibration system for the LA3 camera.

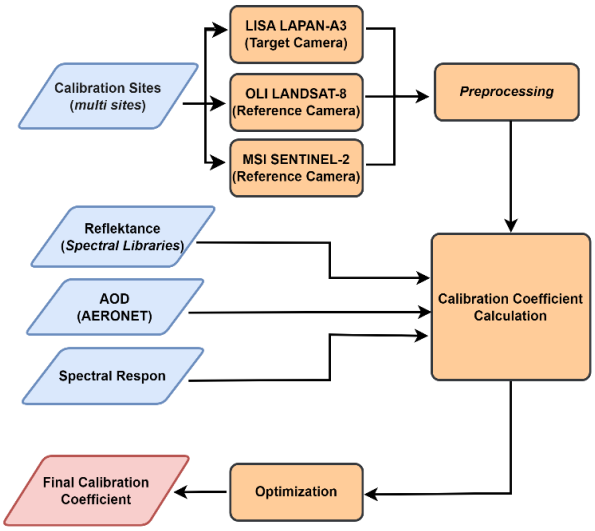

Fig. 1. Block diagram of the multi-site cross-calibration system on the LISA LAPAN-A3 (LA3).

Based on Fig. 1, the first step of this calibration involves LA3 (target camera), OL8, and MS2 (reference cameras) capturing images of the calibration sites at nearly the same time. Next, the cross-calibration method is used for the preprocessing and calibration coefficient calculation steps. This procedure will yield many calibration coefficients. The Kalman filter is used to conduct an optimization process to generate a single final calibration coefficient. The final calibration coefficient is then determined by selecting the coefficient with the smallest error. This process is carried out for each image channel (RGBN).

A. Preprocessing

Before the calibration process, image preprocessing is conducted on both the target and the reference camera images. For the LA3 (target camera) image, as well as the OL8 and MS2 (reference camera) images, the process involves determining the Region of Interest (ROI).

The ROI determination process for LA3 includes setting the ROI boundary coordinates based on the recommendations of the Committee on Earth Observation Satellites (CEOS), identifying ROI points within the ROI boundary, adjusting the ROI points if they do not match the reference cameras, selecting 4 x 4 pixels at each ROI point, and calculating the average Digital Number (DN) of the selected pixels. This average DN will then be processed further.

Meanwhile, for OL8 and MS2, which are the reference cameras, the ROI determination process involves setting the ROI boundary coordinates based on the recommendations of CEOS, identifying ROI points within the ROI boundary, selecting 2 x 2 pixels for OL8 and 6 x 6 pixels for MS2 at each ROI point, and calculating the average DN of the selected pixels to obtain the reference camera DN. The DN values from the target and reference cameras will be used to calculate calibration coefficients.

B. Calculation of Calibration Coefficients

The calculation of calibration coefficients is carried out under the assumption that the response of the LA3 camera is linear. Therefore, the calibration coefficients can be calculated using Eq. (1) [40].

$$\frac{DN_L}{g_L} + o_L = \frac{k.DN_R.c_R.E_L.cos(\theta_L)}{\pi.d^2.cos(\theta_R)} \quad (1)$$

Where DN_L is the DN for LA3, g_L is the calibration gain for LA3, O_L is the calibration offset for LA3, SBAF is the Spectral Band Adjustment Factor (SBAF), DN_R is the digital number of the reference camera, c_R is the calibration gain of the reference camera, E_L is the average solar irradiance for the channel being considered, θ_L is the solar zenith angle for the LA3 camera, d is the average distance between the sun and the Earth, and θ_R is the solar zenith angle for the reference camera. Based on the results of laboratory calibration, the calibration offset for the LA3 camera is 0, so the calibration coefficient (gain) can be obtained using Eq. (2).

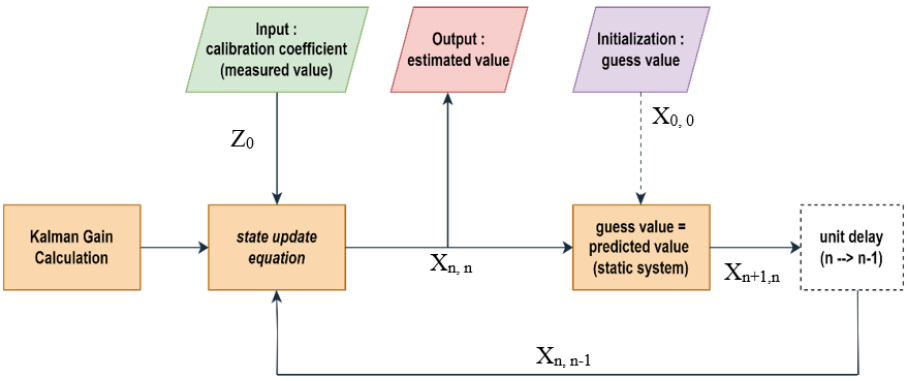

Fig. 2. Block diagram of one-dimensional Kalman filter.

$$g_L = \frac{DN_L . \pi . d^2 . cos(\theta_R)}{SBAF . DN_R . c_R . E_L . cos(\theta_L)} \quad (2)$$

Based on Eq. (2), several inputs and constants are used to obtain the calibration coefficient. DN_L and DN_R are derived from the preprocessing stage. θ_L, θ_R, and c_R come from the image metadata. π, d, and E_L are known constants. Meanwhile, SBAF is a constant obtained from the spectral matching process.

Spectral matching is adjusting spectral responses to account for the differences between the target camera and the reference cameras. This process produces a correction factor known as the Spectral Band Adjustment Factor (SBAF). This correction factor is the ratio of the reflectance of the target camera to that of the reference camera, simulated using MODTRAN software. This process requires inputs such as ground reflectance, aerosol optical depth (AOD), and the spectral response functions of both the target and reference cameras.

The outputs from preprocessing (DNL and DNR), spectral matching (SBAF), and metadata (θL, θR, cR) are then used as inputs for the calculation of the calibration coefficient. The calibration coefficient is calculated based on equation 3.2, resulting in the calibration coefficient (gL). This calculation is carried out for every channel in the LA3 image, yielding a calibration coefficient for each channel (gLR, gLG, gLB, gLN) in the form of a gain factor.

C. Optimization Process

The calibration process will yield many calibration coefficients for each channel. Therefore, an optimization process is needed to obtain the best calibration coefficient. This work uses a one-dimensional Kalman filter to carry out the optimization process. This method is selected because it is anticipated to lower measurement noise, leading to a more accurate radiance measurement by the LA3. Fig. 2 displays the optimization process diagram using the one-dimensional Kalman filter, while Eq. (3) displays the mathematical formula for the output of the one-dimensional Kalman filter.

$$X_{n,n} = X_{n,n-1} + \frac{1}{n}(Z_n - X_{n,n-1}) \quad (3)$$

with

$X_{n,n}$: output (estimated value)

Z_n : measurement value

$X_{0,0}$: predicted value

$X_{n+1,n}$: predicted value

$X_{n,n-1}$: predicted value in the previous process

$\frac{1}{n}$: Kalman gain

The measurement values are the subsequent calibration coefficients obtained from the calibration process, while the initial guess value used is the first calibration coefficient from the measurement process. The calibration coefficient will ultimately be used as the final predicted or estimated value from the optimization process using the one-dimensional Kalman filter.

IV. Result

A. Image Data

This study uses some images with 66 ROI points. The number of ROIs is adjusted based on the image area that can be used for calibration ROI and corresponds to the reference image area. Each image uses 4x4 pixels for the LISA LAPAN-A3 (LA3) image, 2x2 pixels for the OLI LANDSAT-8 (OL8) image, and 6x6 pixels for the MSI SENTINEL-2 (MS2) image, representing a total area of 60x60 meters on the ground. The LA3 images are obtained from the LA3 image database, OL8 images are obtained from the website https://earthexplorer.usgs.gov/, and MS2 images are obtained from the website https://sentinels.copernicus.eu/. The calibration sites and reference image acquisition times are based on the availability of LA3 images. As previously noted, image requirements for calibration are also taken into account. Fig. 3 displays an example of ROI construction on images of the calibration site.

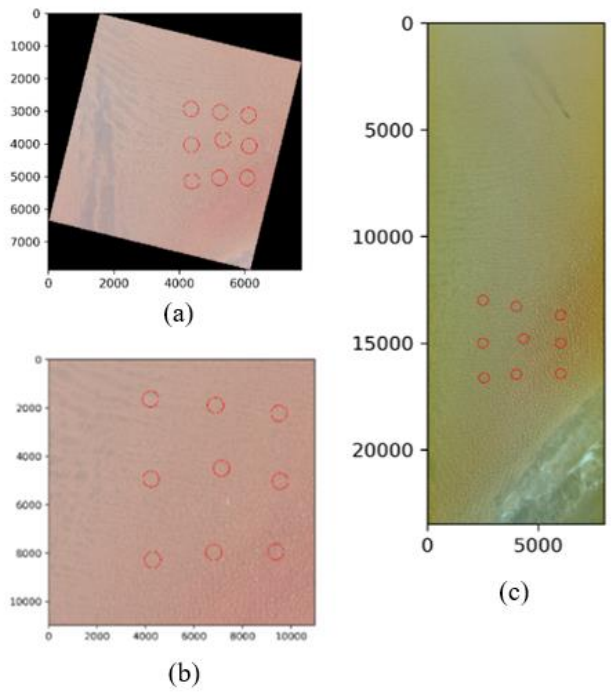

Fig. 3. ROI of Algeria-3 calibration site on imagery citra (a) OL8, (b) MS2, and (c) LA3.

B. Calibration Result

The digital number (DN) for each pixel in each ROI is obtained once the images have been ROI'd. Subsequently, the average DN of the pixels within each ROI is calculated to get a single DN value for each ROI. Every image is subjected to this procedure, including the LA3 image as the target image and OL8 and MS2 as the reference images.

The next step is spectral matching, which yields a spectral band adjustment factor (SBAF). The SBAF for each channel at different calibration sites is shown in Table III and Table IV.

TABLE III. SBAF LA3 AGAINST OL8 AND LA3 AT CALIBRATION SITE

Num	Sites	LA3-OL8			
		R	G	B	N
1	Libya 1	1,026	0,825	0,813	0,988
2	Mauritania 1	0,981	0,837	0,817	0,966
3	Mauritania 2	0,981	0,837	0,817	0,966
4	Libya 4	1,026	0,825	0,813	0,988
5	Algeria 3	1,026	0,825	0,813	0,988
6	La Crau	1,021	0,918	0,835	0,955

TABLE IV. SBAF LA3 AGAINST MS2 AND LA3 AT CALIBRATION SITE

Num	Sites	LA3-MS2			
		R	G	B	N
1	Libya 1	1,004	0,854	0,835	0,998
2	Mauritania 1	0,996	0,870	0,854	0,960
3	Mauritania 2	0,996	0,870	0,854	0,960
4	Libya 4	1,004	0,854	0,835	0,998
5	Algeria 3	1,004	0,854	0,835	0,998
6	La Crau	1,007	0,923	0,847	0,996

Based on Table III and Table IV, it can be seen that spectral differences between LA3 and OL8, as well as between LA3 and MS2, are not very significant, especially in the red and NIR channels. The SBAF results, which get close to 1 at a few calibration sites, make this clear. However, in the green channel (G), both LA3-OL8 and LA3-MS2 show lower SBAF values than the red and NIR channels. When considering each calibration site, La Crau has the best SBAF values in every channel compared to other sites.

After obtaining the SBAF values, the calibration coefficient calculation process is carried out. Calibration coefficients are derived using this procedure to convert the LA3 image's DN values into radiance. In this study, two types of calibration coefficients will be obtained: the calibration coefficient with OL8 as the reference and the calibration coefficient with MS2 as the reference. Fig. 4 and 5 display the calibration coefficients for each ROI at multiple calibration sites.

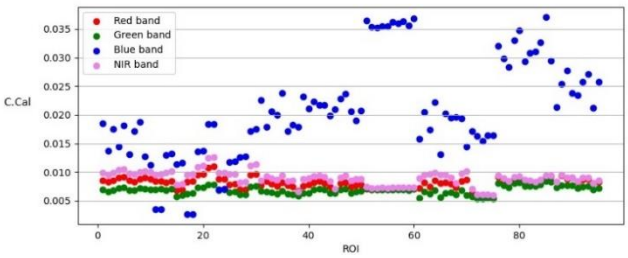

Fig. 4. Calibration coefficient of LA3 with reference OL8.

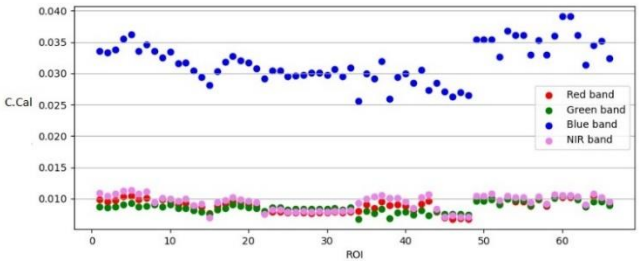

Fig. 5. Calibration coefficient of LA3 with reference MS2.

TABLE V. THE ROI NUMBERS FOR THE CALIBRATION SITES

Calibration of LA3 with Reference OL8		Calibration of LA3 with Reference MS2	
ROI	Calibration Site	ROI	Calibration Site
1-10	Libya 1	1-7	Libya 1
11-30	Algeria 5	8-17	Mauritania 1
31-40	Mauritania 1	18-22	Mauritania 2
41-50	Mauritania 2	23-33	Libya 4
51-60	Libya 4	34-43	Algeria 3
61-70	Algeria 3	44-48	La Crau
71-75	La Crau	49-61	Mauritania 1
76-85	Mauritania 1	62-66	Mauritania 2
86-95	Mauritania 2		

Fig. 4 shows the calibration coefficients of LA3 with OL8 as the reference, and Fig. 5 shows the calibration coefficients of LA3 with MS2 as the reference. Meanwhile, Table V shows the ROI numbers for the calibration sites used in Fig. 4 and 5. It is evident from both figures that the calibration coefficients vary across different calibration sites and different periods. If the averaging process is carried out based on on-site calibration and time, then a graph is obtained in Fig. 6 to 9.

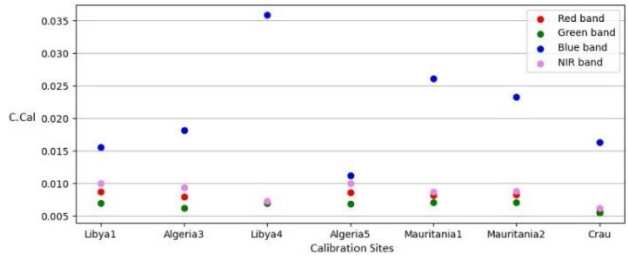

Fig. 6. Average LA3 calibration coefficient with OL8 reference at each calibration site.

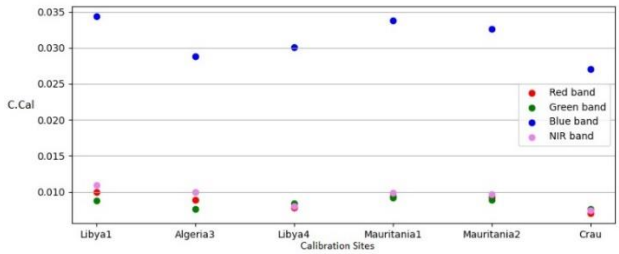

Fig. 7. Average LA3 calibration coefficient with MS2 reference at each calibration site.

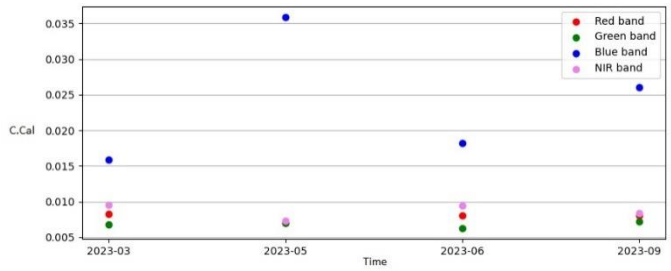

Fig. 8. Average LA3 calibration coefficient with OL8 reference based on time.

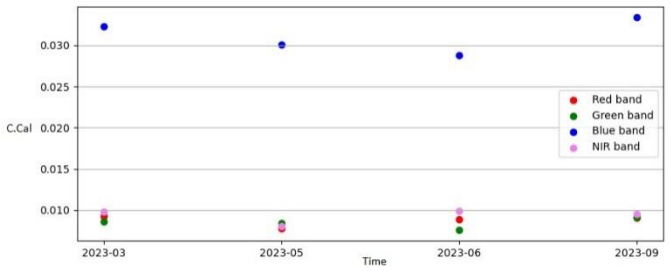

Fig. 9. Average LA3 calibration coefficient with MS2 reference based on time.

Fig. 6 shows the average calibration coefficient graph of LA3 with OL8 as the reference across different ROIs representing specific calibration sites. From the figure, it is evident that the red and NIR channels tend to remain stable in Libya 1, Algeria 3, Algeria 5, Mauritania 1, and Mauritania 2. The red channel ranges from 0.0080 to 0.0087, while the NIR channel ranges from 0.0087 to 0.0099. At Libya 4, the red and NIR channels are slightly lower than at other calibration sites in the Sahara Desert, but the blue channel is the highest compared to other sites. The calibration coefficients at this site are 0.007 for the red and green channels, 0.035 for the blue channel, and 0.0073 for the NIR channel. At La Crau, the red, green, and NIR channels are lower than at other calibration sites. Meanwhile, the calibration coefficient for the blue channel is lower than at other calibration sites, except for Libya 1. The calibration coefficients at this site are 0.0057 for the red channel, 0.0054 for the green channel, 0.016 for the blue channel, and 0.0062 for the NIR channel.

Fig. 7 shows the average calibration coefficient graph of LA3 with MS2 as the reference across different ROIs representing specific calibration sites. From the figure, it is evident that the red and NIR channels tend to remain stable in Libya 1, Algeria 3, Algeria 5, Mauritania 1, and Mauritania 2. The calibration coefficients range from 0.0088 to 0.0099 for the red channel and from 0.0091 to 0.011 for the NIR channel. The calibration coefficient for the green channel remains relatively stable across all calibration sites, ranging from 0.0076 to 0.0089. At Libya 4, the red and NIR channels are slightly lower than at other calibration sites in the Sahara Desert, with values of 0.0078 for the red channel and 0.0080 for the NIR channel. At La Crau, the red, green, blue, and NIR channels are lower than at other calibration sites. Meanwhile, the blue channel tends to be more stable than the calibration using OL8 as a reference, with values ranging from 0.026 to 0.034. This differs from the calibration using OL8 as a reference, where the blue channel is more fluctuating, with values ranging from 0.0080 to 0.035.

Fig. 8 shows the average calibration coefficient of LA3 with OL8 as the reference based on time. It can be observed that the red and green channel tends to remain stable in March, May, June, and September. In the NIR channel, there is a slight decrease in May and September compared to March and June. Meanwhile, the blue channel fluctuates, with values ranging from 0.015 to 0.035. Fig. 9 shows the average calibration coefficient of LA3 with OL8 as the reference over time. The figure indicates that the red and blue channels tend to be stable, with values ranging from 0.0078 to 0.0092 for the red channel and 0.028 to 0.032 for the blue channel. In March, there is a decrease in the calibration coefficient for the NIR channel, and in June, there is a decrease in the green channel.

C. Optimization Result

After obtaining the calibration coefficients, an optimization is carried out to derive a final calibration coefficient close to the reference value. The optimization is performed using a Kalman filter. Fig. 10 through 17 display the calibration coefficient optimization outcomes using the Kalman filter.

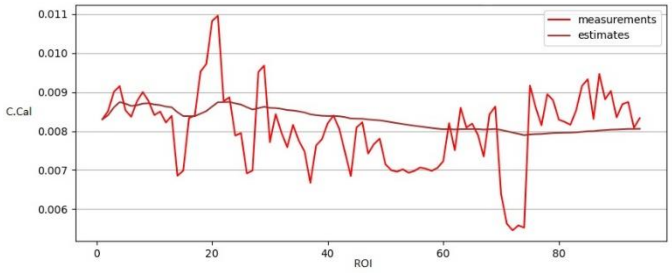

Fig. 10. Calibration coefficients optimization result of LA3 reference OL8 with one-dimensional Kalman filter on red channel.

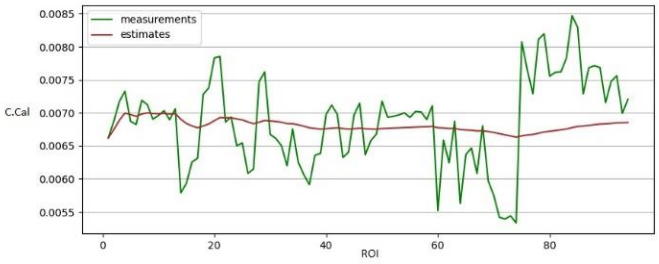

Fig. 11. Calibration coefficients optimization result of LA3 reference OL8 with one-dimensional Kalman filter on green channel.

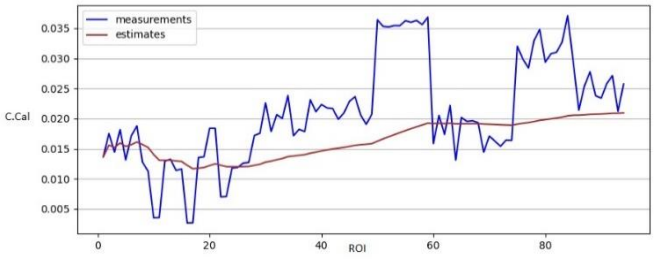

Fig. 12. Calibration coefficients optimization result of LA3 Reference OL8 with one-dimensional Kalman filter on blue channel.

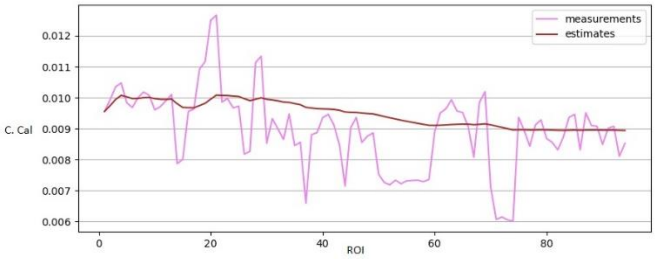

Fig. 13. Calibration coefficients optimization result of LA3 reference OL8 with one-dimensional Kalman filter on nir channel.

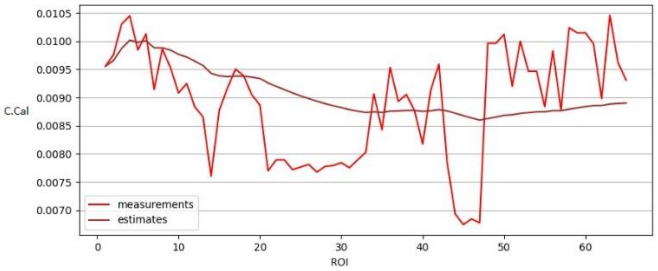

Fig. 14. Calibration coefficients optimization result of LA3 reference MS2 with one-dimensional Kalman filter on red channel.

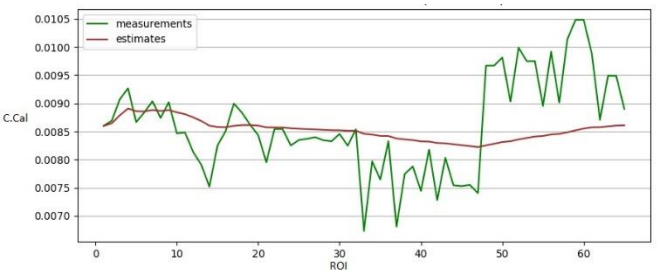

Fig. 15. Calibration coefficients optimization result of LA3 reference MS2 with one-dimensional Kalman filter on green channel.

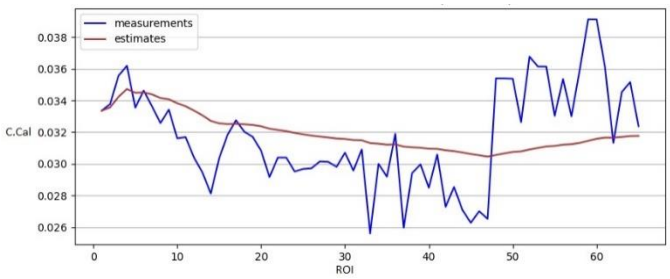

Fig. 16. Calibration coefficients optimization result of LA3 reference MS2 with one-dimensional Kalman filter on blue channel.

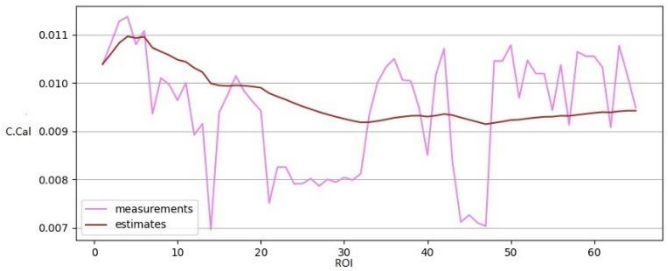

Fig. 17. Calibration coefficients optimization result of LA3 reference MS2 with one-dimensional Kalman filter on nir channel.

Fig. 10 to 13 show the comparison graphs of the LA3 calibration coefficients referenced to OL8 before and after optimization using the Kalman filter. It can be seen that these graphs experience a reduction in fluctuations, and the graphs resulting from the Kalman filter optimization tend to be more stable for each sample area. The final results of this optimization process are 0.0081 for the red channel, 0.0069 for the green channel, 0.02 for the blue channel, and 0.0089 for the NIR channel. Subsequently, these calibration coefficients will be cross-validated using MS2 imagery.

Meanwhile, Fig. 14 to 17 present the comparison graphs of the LA3 calibration coefficients referenced to MS2 before and after optimization using the Kalman filter. It can be observed that these graphs also show a reduction in fluctuations, and the graphs resulting from the Kalman filter optimization tend to be more stable for each sample area. The final results of this optimization process are 0.0089 for the red channel, 0.0086 for the green channel, 0.032 for the blue channel, and 0.0094 for the NIR channel. Subsequently, these calibration coefficients will be cross-validated using OL8 imagery.

D. Validation and Evaluation

The Digital Number (DN) can be converted into radiance using the calibration coefficients that were obtained during the calibration procedure. The first validation stage was performed using the same data and calibration sites as in the calibration process. However, the validation was carried out crosswise, i.e. validating LA3 radiance referenced to OL8 with MS2 radiance and validating LA3 radiance referenced to MS2 with OL8 radiance. This process was conducted on pre- and post-optimization data to assess the difference between LA3 radiance and the radiance of standardized satellites. The validation graphs of LA3 radiance with OL8 reference compared to MS2 radiance are shown in Fig. 18 to 21.

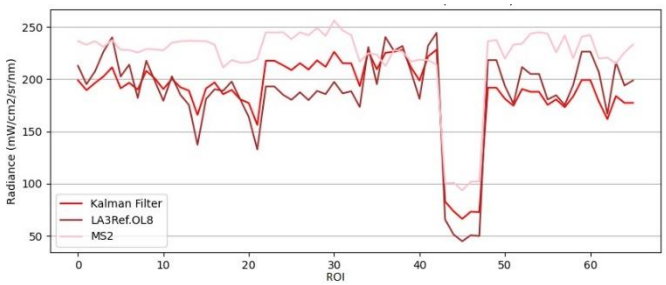

Fig. 18. Validation graph of LA3 radiance with OL8 reference before and after optimization on red channel compared to MS2 radiance.

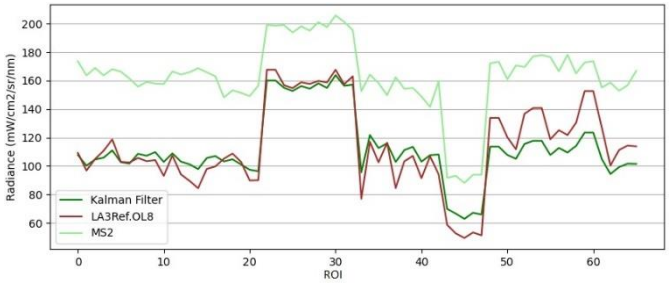

Fig. 19. Validation graph of LA3 radiance with OL8 reference before and after optimization on green channel compared to MS2 radiance.

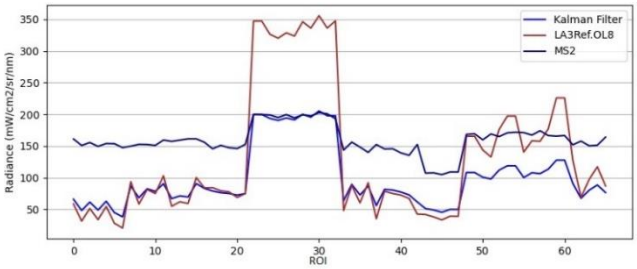

Fig. 20. Validation graph of LA3 radiance with OL8 reference before and after optimization on blue channel compared to MS2 radiance.

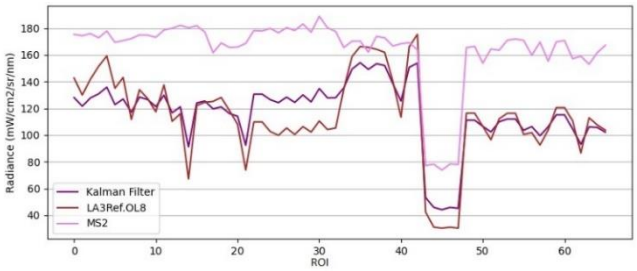

Fig. 21. Validation graph of LA3 radiance with OL8 reference before and after optimization on nir channel compared to MS2 radiance.

TABLE VI. PERCENTAGE DIFFERENCE IN LA3 RADIANCE WITH OL8 REFERENCE COMPARED TO MS2 RADIANCE

Sites	ROI	Percentage Difference in LA3 Radiance with OL8 Reference Compared to MS2 Radiance (%)							
		Before Optimization				After Optimization			
		R	G	B	N	R	G	B	N
Lib1	1-7	8.05	36.03	74.05	17.52	14.92	37.05	65.46	26.52
Mau1	8-17	20.44	39.72	50.58	34.20	17.19	35.25	49.52	32.29
Mau2	18-22	20.04	34.52	48.18	33.34	17.68	33.72	49.14	32.18
Lib4	23-33	23.34	18.99	70.31	41.54	12.11	20.88	0.72	28.71
Alg3	34-43	1.66	35.33	54.79	8,11	1.392	29.38	49.08	13.12
LCr	44-48	47.38	42.43	64.42	57,13	26.07	27.88	54.39	39.19
Mau12	49-61	14.60	23.07	3.58	34.01	21.08	33.68	33.73	34.44
Mau22	62-66	11.82	28.31	35.78	44.31	21.10	36.54	47.96	45.73

Fig. 18 to 21 show the validation graphs of LA3 with OL8 reference before and after optimization using the one-dimensional Kalman filter. MS2 radiance, the other reference camera, is used to compare radiance before and after optimization. The figures indicate that some lines get closer to the reference radiance line after optimization with the one-dimensional Kalman filter. However, some lines move further away after the optimization process. Based on Table VI, five sites in the red channel show a decrease in percentage difference, while three sites show an increase. In the green, blue, and NIR channels, four sites show a decrease in percentage difference, and four sites show an increase. Next, the radiance of LA3 with MS2 reference before and after optimization is compared to OL8 radiance. Fig. 22 to 25 are the validation graphs from this process.

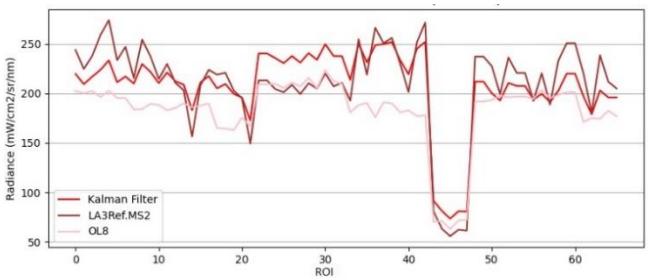

Fig. 22. Validation graph of LA3 radiance with MS2 reference before and after optimization on red channel compared to OL8 radiance.

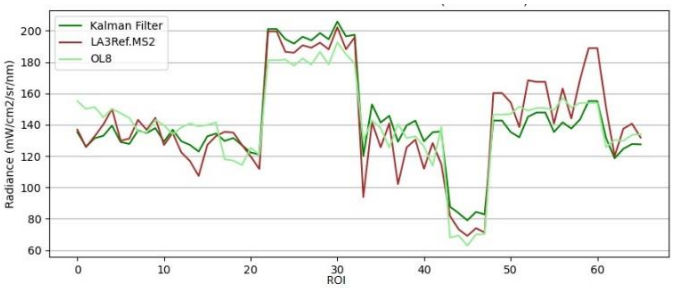

Fig. 23. Validation graph of LA3 radiance with MS2 reference before and after optimization on green channel compared to OL8 radiance.

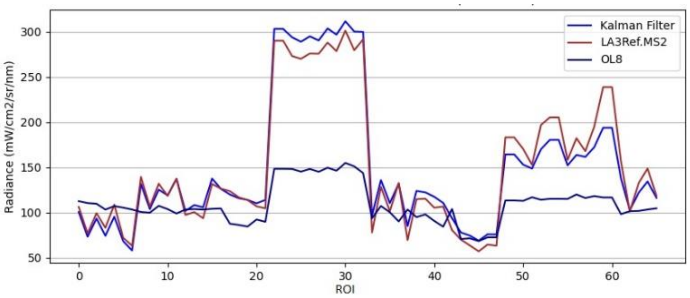

Fig. 24. Validation graph of LA3 radiance with MS2 reference before and after optimization on blue channel compared to OL8 radiance.

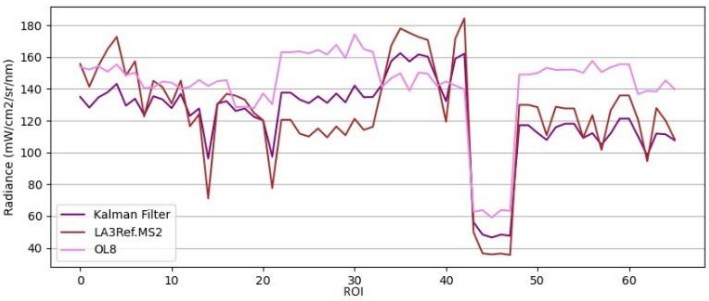

Fig. 25. Validation graph of LA3 radiance with MS2 reference before and after optimization on nir channel compared to OL8 radiance.

TABLE VII. PERCENTAGE DIFFERENCE IN LA3 RADIANCE WITH MS2 REFERENCE COMPARED TO OL8 RADIANCE

Sites	ROI	Percentage Difference in LA3 Radiance with MS2 Reference Compared to OL8 Radiance (%)							
		Before Optimization				After Optimization			
		R	G	B	N	R	G	B	N
Lib1	1-7	23.36	9.26	62.93	2.81	9.83	11.64	25.16	11.54
Mau 1	8-17	15.37	6.82	24.93	11.58	13.85	4.74	16.27	11.35
Mau 2	18-22	18.33	5.64	12.39	9.36	17.79	6.03	30.40	9.03
Lib4	23-33	1.08	5.70	128.42	29.94	12.85	8.36	101,90	17.77
Alg3	34-43	30.49	7.88	31.64	12.59	30.58	3.99	16.75	6.65
LCr	44-48	7.04	8.53	46.05	37.85	17.25	22.67	4.86	20.96
Mau 12	49-61	13.95	7.65	50.76	18.38	4.35	5.08	46.26	24.88
Mau 22	62-66	20.02	4.27	2.03	18.22	10.32	3.53	20.38	22.85

Fig. 22 to 25 show the validation graphs of LA3 with MS2 reference before and after optimization using the one-dimensional Kalman filter. The other reference camera, OL8, is used to compare the radiation levels before and after optimization. The figures indicate that some lines get closer to the reference radiance line after optimization with the one-dimensional Kalman filter. However, following the optimization procedure, certain lines get farther apart. Furthermore, the Libya-4 site exhibits a noteworthy percentage variation in the blue channel. Based on Table VII, in the red, green, and NIR channels, five sites show a decrease in percentage difference, while three sites show an increase in percentage difference. In the blue channel, six sites show a decrease in percentage difference, and two sites show an increase in percentage difference.

V. DISCUSSION

Based on the results, in the preprocessing stage of this study, digital numbers (DN) were derived for each image: LA3, OL8, and MS2. Subsequently, SBAF calculations were performed. The results show that the SBAF values in the RGBN channels are close to 1 (Tables III and IV). This indicates that the spectral response of LA3 is similar to that of the reference cameras (OL8 and MS2). Once the SBAF values were obtained, calibration coefficients could be calculated using DN, SBAF, reflectance, and AOD. From this process, calibration coefficients are shown in Fig. 4 and 5. The graph indicates that the blue channel's calibration coefficient is higher than the other channels. This is because the digital number for the blue channel is lower than the other channels, requiring a high calibration coefficient to reach the reference radiance value.

The calibration coefficients obtained during the calculation process showed fluctuations across each ROI, whereas, in theory, they should have similar values at the calibration site. Therefore, this study used a Kalman Filter to reduce noise in the calibration coefficients. Furthermore, the Kalman Filter was employed to optimize the calibration coefficients, resulting in a single calibration coefficient value. These values are used to convert DN to TOA radiance.

Based on the results, the optimization process using the Kalman Filter reduce noise in the calibration coefficient graphs (Fig. 10 until Fig. 17). This can be seen from the calibration coefficient graphs, which initially showed fluctuations but became more stable for each ROI. The calibration coefficients for LA3 with OL8 and MS2 reference were obtained from the optimization. The calibration coefficient for LA3 with OL8 reference is 0.0081 for the red channel, 0.0069 for the green channel, 0.02 for the blue channel, and 0.0089 for the NIR channel. The calibration coefficient of LA3 with MS2 reference are 0.0089 for the red channel, 0.0086 for the green channel, 0.032 for the blue channel, and 0.0094 for the NIR channel. Next, these calibration coefficients were validated using another reference camera as the validator. The calibration coefficient for LA3 with OL8 reference was validated with MS2, while the calibration coefficient for LA3 with MS2 reference was validated with OL8.

The cross-validation results show that the LA3 calibration process with MS2 as the reference results in radiance values closer to the reference radiance than OL8 as the reference. This implies that using MS2 as the reference camera is more sensible for the LA3 cross-calibration procedure. This calibration technique demonstrates that, for most images, the red, green, blue, and NIR channels can be effectively optimized with a one-dimensional Kalman filter. However, further development is needed to achieve better results. Extended Kalman Filter (EKF), Unscented Kalman Filter (UKF), or other methods can be considered for further research so that the radiance produced from the cross-calibration process more closely matches the reference radiance values.

VI. CONCLUSION

The multi-site cross-calibration method with one-dimensional Kalman filter optimization can be implemented on the LA3 camera. It is possible to optimize calibration coefficients using the one-dimensional Kalman Filter, as can be inferred from the discussion in the preceding section. This is evident from the reduction in the percentage difference between LA3 radiance and reference radiance after the optimization process. The results also show that LA3 calibration process with MS2 as the reference results in radiance values closer to the reference radiance than OL8 as the reference. This implies that using MS2 as the reference camera is more sensible for the LA3 cross-calibration procedure. Basically, this method can be applied on LA3. However, further development is needed to achieve better results so that the radiance produced from the cross-calibration process more closely matches the reference radiance values.

ACKNOWLEDGMENT

The author would like to thank Mr. Mohammad Mukhayadi and Mr. Patria Rachman Hakim as group leader and leader satellite operation missions of Satellite Technology Research Center BRIN, for their support and assistance so that this works can be well completed.

REFERENCES

[1] P. R. Hakim, A. H. Syafrudin, S. Salaswati, S. Utama, and W. Hasbi, "Development of Systematic Image Preprocessing of LAPAN-A3/IPB Multispectral Images," vol. 7, no. 10, pp. 9–18, 2019, [Online]. Available: http://arxiv.org/abs/1901.09189.

[2] S. Bolívar-Santamaría and B. Reu, "Detection and characterization of agroforestry systems in the Colombian Andes using sentinel-2 imagery," *Agrofor. Syst.*, vol. 95, no. 3, pp. 499–514, 2021, doi: 10.1007/s10457-021-00597-8.

[3] M. T. Parveen and R. A. Ilahi, "Assessment of land-use change and its impact on the environment using GIS techniques: a case of Kolkata Municipal Corporation, West Bengal, India," *GeoJournal*, vol. 87, no. s4, pp. 551–566, 2022, doi: 10.1007/s10708-022-10581-z.

[4] H. Fadaei, "Advanced land observing satellite data to identify ground vegetation in a juniper forest, northeast Iran," *J. For. Res.*, vol. 31, no. 2, pp. 531–539, 2020, doi: 10.1007/s11676-018-0812-5.

[5] A. Sharifi, S. Felegari, and A. Tariq, "Mangrove forests mapping using Sentinel-1 and Sentinel-2 satellite images," *Arab. J. Geosci.*, vol. 15, no. 20, 2022, doi: 10.1007/s12517-022-10867-z.

[6] C. C. Liu, Y. H. Chen, M. H. M. Wu, C. Wei, and M. H. Ko, "Assessment of forest restoration with multitemporal remote sensing imagery," *Sci. Rep.*, vol. 9, no. 1, pp. 1–19, 2019, doi: 10.1038/s41598-019-43544-5.

[7] M. Tamang, S. Nandy, R. Srinet, A. K. Das, and H. Padalia, "Bamboo Mapping Using Earth Observation Data: A Systematic Review," *J. Indian Soc. Remote Sens.*, vol. 50, no. 11, pp. 2055–2072, 2022, doi: 10.1007/s12524-022-01600-0.

[8] A. D. Prasad, P. Ganasala, R. Hernández-Guzmán, and F. Fathian, "Remote sensing satellite data and spectral indices: an initial evaluation for the sustainable development of an urban area," *Sustain. Water Resour. Manag.*, vol. 8, no. 1, pp. 1–16, 2022, doi: 10.1007/s40899-022-00607-2.

[9] A. K. Wijayanto, S. M. Yusuf, and W. A. Pambudi, "The Characteristic of spectral reflectance of LAPAN-IPB (LAPAN-A3) Satellite and Landsat 8 over agricultural area in Probolinggo, East Java," *IOP Conf. Ser. Earth Environ. Sci.*, vol. 284, no. 1, 2019, doi: 10.1088/1755-1315/284/1/012004.

[10] L. F. Amalo, I. A. Nur, and N. R. Rochimawati, "Drought monitoring using LISAT (LAPAN-IPB Satellite) and Landsat 8 Satellite Imagery in Pakisjaya District, West Java," *IOP Conf. Ser. Earth Environ. Sci.*, vol. 284, no. 1, 2019, doi: 10.1088/1755-1315/284/1/012008.

[11] P. A. Permatasari, S. Muslimah, and B. A. Utomo, "Comparison of LISAT and Landsat imagery for estimating chlorophyll-a (case study: Jatiluhur Reservoir)," *IOP Conf. Ser. Earth Environ. Sci.*, vol. 284, no. 1, 2019, doi: 10.1088/1755-1315/284/1/012041.

[12] M. A. Raimadoya, B. H. Trisasongko, and A. Zain, "Analisis Misi Dan Rancangan Lapan-Ipb Satellite (Lisat) Untuk Pemantauan Kemandirian Pangan," *J. Ilmu Pertan. Indones.*, vol. 16, no. 3, pp. 173–178, 2011.

[13] S. P. Nugroho, L. D. W. Handayani, R. Meidiza, and G. Munggaran, "Landuse change analysis for hydrology response and planning management of Cibeet Sub-Watershed, West Java, Indonesia," *IOP Conf. Ser. Earth Environ. Sci.*, vol. 284, no. 1, 2019, doi: 10.1088/1755-1315/284/1/012002.

[14] Q. Hao *et al.*, "The Development of Snapshot Multispectral Imaging Technology Based on Artificial Compound Eyes," *Electron.*, vol. 12, no. 4, 2023, doi: 10.3390/electronics12040812.

[15] Q. Song *et al.*, "Time Series Analysis-Based Long-Term Onboard Radiometric Calibration Coefficient Correction and Validation for the HY-1C Satellite Calibration Spectrometer," *Remote Sens.*, vol. 14, no. 19, 2022, doi: 10.3390/rs14194811.

[16] K. Arai, "Comparison Among Cross, Onboard and Vicarious Calibrations for Terra/ASTER/VNIR," *Int. J. Adv. Res. Artif. Intell.*, vol. 2, no. 10, pp. 14–18, 2013, doi: 10.14569/ijarai.2013.021003.

[17] S. Zhu *et al.*, "In-Flight Relative Radiometric Calibration of a Wide Field of View Directional Polarimetric Camera Based on the Rayleigh Scattering over Ocean," *Remote Sens.*, vol. 14, no. 5, pp. 1–19, 2022, doi: 10.3390/rs14051211.

[18] S. Zhu *et al.*, "Evaluation of radiometric performance of MODIS visible bands using the Rayleigh scattering method," *J. Appl. Remote Sens.*, vol. 13, no. 01, p. 1, 2019, doi: 10.1117/1.jrs.13.018503.

[19] X. Chen *et al.*, "In-flight calibration of GF-1/WFV visible channels using Rayleigh scattering," *Remote Sens.*, vol. 9, no. 6, 2017, doi: 10.3390/rs9060513.

[20] K. Tan *et al.*, "Vicarious Calibration for the AHSI Instrument of Gaofen-5 with Reference to the CRCS Dunhuang Test Site," *IEEE Trans. Geosci. Remote Sens.*, vol. 59, no. 4, pp. 3409–3419, 2021, doi: 10.1109/TGRS.2020.3014656.

[21] B. Alhammoud *et al.*, "Sentinel-2 Level-1 Radiometry Assessment Using Vicarious Methods from DIMITRI Toolbox and Field Measurements from RadCalNet Database," *IEEE J. Sel. Top. Appl. Earth Obs. Remote Sens.*, vol. 12, no. 9, pp. 3470–3479, 2019, doi: 10.1109/JSTARS.2019.2936940.

[22] K. N. Babu, N. Kumawat, and M. R. Pandya, "Radiometric Calibration of AVIRIS-NG sensor using Indian desert sites," *Adv. Sp. Res.*, no. xxxx, 2023, doi: 10.1016/j.asr.2023.01.022.

[23] H. Tang, J. Xie, W. Chen, H. Zhang, and H. Wang, "Absolute Radiometric Calibration of ZY3-02 Satellite Multispectral Imager Based on Irradiance-Based Method," 2023.

[24] J. Lu, T. He, S. Liang, and Y. Zhang, "An Automatic Radiometric Cross-Calibration Method for Wide-Angle Medium-Resolution Multispectral Satellite Sensor Using Landsat Data," *IEEE Trans. Geosci. Remote Sens.*, vol. 60, pp. 1–11, 2022, doi: 10.1109/TGRS.2021.3067672.

[25] C. Gao *et al.*, "Radiometric Cross-Calibration of GF-4 / VNIR Sensor," vol. 13, pp. 2337–2350, 2020.

[26] H. Gao, "Cross-Calibration of GF-1 PMS Sensor With," vol. 54, no. 8, pp. 4847–4854, 2016.

[27] J. Han, Z. Tao, Y. Xie, Q. Liu, and Y. Huang, "Radiometric Cross-Calibration of GF-4/PMS Based on Radiometric Block Adjustment," *IEEE Trans. Geosci. Remote Sens.*, vol. 59, no. 6, pp. 4522–4534, 2021, doi: 10.1109/TGRS.2020.3009740.

[28] H. Mizuochi, S. Tsuchida, K. Obata, H. Yamamoto, and S. Yamamoto, "Combination of cross-and inter-band radiometric calibrations for a hyperspectral sensor using model-based spectral band adjustment," *Remote Sens.*, vol. 12, no. 12, 2020, doi: 10.3390/rs12122011.

[29] K. Arai, "Vicarious Calibration Based Cross Calibration of Solar Reflective Channels of Radiometers Onboard Remote Sensing Satellite and Evaluation of Cross Calibration Accuracy through Band-to-Band Data Comparisons," *Int. J. Adv. Comput. Sci. Appl.*, vol. 4, no. 3, pp. 7–14, 2013, doi: 10.14569/ijacsa.2013.040312.

[30] A. H. Syafrudin, S. Salaswati, and W. Hasbi, "Pre-Flight Radiometric Model of Linear Imager on LAPAN-IPB Satellite," *IOP Conf. Ser. Earth Environ. Sci.*, vol. 149, no. 1, 2018, doi: 10.1088/1755-1315/149/1/012068.

[31] K. Arai *et al.*, "Method for uncertainty evaluation of vicarious calibration of spaceborne visible to near infrared radiometers," *Int. J. Adv. Comput. Sci. Appl.*, vol. 10, no. 1, pp. 387–393, 2019, doi: 10.14569/IJACSA.2019.0100151.

[32] S. Salaswati, P. R. Hakim, A. H. Syafrudin, R. Hartono, and S. Utama, "Vicarious Radiometric Calibration of Lapan-A3 / IPB Satellite Multispectral Imager in Jaddih Hill Madura," *J. Aerosp. Technol.*, pp. 31–42, 2020.

[33] S. Salaswati, P. R. Hakim, A. H. Syafrudin, R. Hartono, and S. Utama, "Analysis of the Atmospheric Effects on the Vicarious Calibration of LAPAN-A3/IPB Satellite Multispectral Camera in Jaddih Hill Madura," *J. Aerosp. Technol.*, vol. 20, no. 1, pp. 55–67, 2022.

[34] C. Bacour, X. Briottet, F. M. Bréon, F. Viallefont-Robinet, and M. Bouvet, "Revisiting Pseudo Invariant Calibration Sites (PICS) over sand deserts for vicarious calibration of optical imagers at 20 km and 100 km scales," *Remote Sens.*, vol. 11, no. 10, pp. 1–28, 2019, doi: 10.3390/rs11101166.

[35] CEOS, "Radiometric Calibration Network Portal." https://www.radcalnet.org/#!/.

[36] C. Revel *et al.*, "Sentinel-2A and 2B absolute calibration monitoring," *Eur. J. Remote Sens.*, vol. 52, no. 1, pp. 122–137, 2019, doi: 10.1080/22797254.2018.1562311.

[37] M. A. Ridwan *et al.*, "Applications of landsat-8 data: A Survey," *Int. J. Eng. Technol.*, vol. 7, no. 4, pp. 436–441, 2018, doi: 10.14419/ijet.v7i4.35.22858.USGS, "What are the best Landsat spectral bands for use in my research?" https://www.usgs.gov/faqs/what-are-best-landsat-spectral-bands-use-my-research (accessed Jun. 10, 2023).

[38] E. S. Agency, *Sentinel-2 User Handbook*. ESA Standard Document, 2015.

[39] L. Liu, T. Shi, H. Gao, X. Zhang, Q. Han, and X. Hu, "Long-term cross calibration of HJ-1A CCD1 and Terra MODIS reflective solar bands," *Sci. Rep.*, vol. 11, no. 1, pp. 1–14, 2021, doi: 10.1038/s41598-021-86619-y.